Electronic Supplementary Information for: Multi-Scale Approach for Modeling Stability, Aggregation, and Network Formation of Nanoparticles Suspended in Aqueous Solutions

Annalisa Cardellini[1,2], Matteo Alberghini[1], Ananth Govind Rajan[2], Rahul P. Misra[2], Daniel Blankschtein[2], and Pietro Asinari[1*]*

[1]Department of Energy, Politecnico di Torino, Torino, Italy
[2]Department of Chemical Engineering, Massachusetts Institute of Technology, Cambridge, Massachusetts 02139, United States
E-mail: dblank@mit.edu; pietro.asinari@polito.it
* Corresponding Authors

Electronic Supplementary Information Contents

1. Alumina Nanoparticle (NP) Design and Force Fields

A unit cell of α-Al_2O_3 (110) was considered to begin designing the atomistic model of the NP (leftmost picture of Fig. S1). This unit cell is first replicated along all Cartesian axes, in order to build a fully periodic brick of 10 x 10 x 5 nm^3 (see the middle picture in Fig. S1). Then, a spherical particle is obtained by retaining only atoms within a fixed distance from the brick center (radius), as shown in the rightmost picture of Fig. S1. Two separate NPs are designed by the previous procedure, one

with a radius of 2 nm, and the other one with a 0.85 nm radius. Because we aim to study the alumina nanoparticle in hydrated environments, the α-Al_2O_3 surfaces have been modeled using the methodology described below. Note that we focus on alumina because of the broad range of technological applications where it is used. The chemical resistance and porosity of alumina surfaces enable superior performance when it is used as a catalyst or catalyst support[S1]. Moreover, alumina is largely utilized as a dielectric in microelectronics[S2], and because of its relatively high thermal conductivity, α-Al_2O_3 is one of the few ceramic materials to be largely employed in thermal nanofluids[S3,S4].

Numerous investigations have demonstrated the presence of hydroxylation phenomena occurring in the surface chemistry of alumina[S5-S7]. For example, Eng *et al*. experimentally studied the surface properties of the hydrated α-Al_2O_3 (0001) surface and showed an oxygen-terminated surface with the formation of some ordered water layers at the solid-liquid interface[S8]. Therefore, the α-Al_2O_3 nanoparticles, previously obtained, have been functionalized by adding OH terminal groups. Specifically, the surface aluminium atoms with less than 6 bonds are eliminated from the structure, and the hydrogen atoms are bonded to some surface oxygens, fixing the O-H bond to 0.96 nm and the Al-O-H angle to 168° with a random azimuth angle. Because the extent of hydroxylation is found to decrease with nanoparticle size[S9], the number of OH groups has been tuned from ~ 2.6 OH/nm^2 to ~ 7.6 OH/nm^2, where the solvent accessible surface area[S10] has been considered in the calculation.

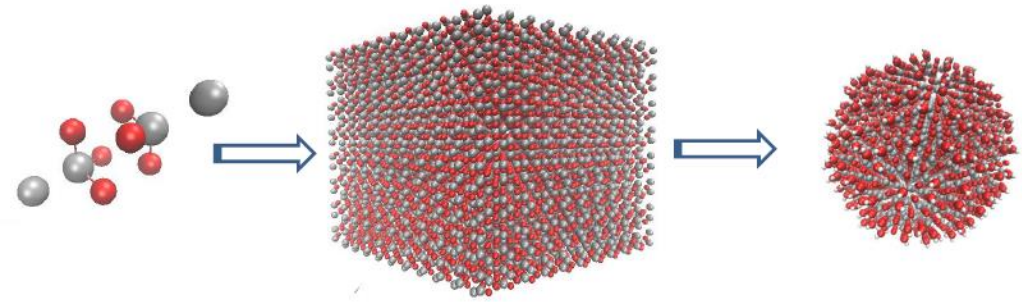

Fig. S1: Preparation of the MD geometry of the crystal alumina NP. From left to right: unit cell of alumina (α-Al_2O_3), alumina crystal brick (10 x 10 x 5 nm^3), alumina NP having a 4 nm diameter including surface hydroxylation. Color code: aluminium atoms are depicted in gray, oxygen atoms are depicted in red, and hydrogen atoms are depicted in white.

The atomistic structure of alumina is described by implementing the CLAYFF force field developed by Cygan *et al*. [S11]. All the bonds and angles within the NP core are modeled with harmonic potentials whose parameters can be found in reference[S11]. Further, Lennard-Jones (LJ) and Coulomb (C) interaction potentials were imposed to model the dispersion and electrostatic interactions, respectively. Specifically,

$$U_{NON-BOND} = U_{LJ} + U_C = 4\varepsilon_{ij}\left[\left(\frac{\sigma_{ij}}{r_{ij}}\right)^{12} - \left(\frac{\sigma_{ij}}{r_{ij}}\right)^{6}\right] + \frac{1}{4\pi\epsilon_0}\frac{q_i q_j}{r_{ij}}, \quad (1)$$

where q_i and q_j are the partial charges on atoms i and j, respectively, r_{ij} is the distance between atoms i and j, and ϵ_0 is the permittivity of free space. Partial charges were only assigned to the surface atoms belonging to the Al-O-H groups, whereas zero charges (i.e., $q_i = 0$) were imposed on

the bulk atoms. Both the partial charges and the LJ parameters of each atom in the NP, including the OH termination, are consistent with the CLAYFF force field[S11], and are reported in Table S1.

In order to evaluate the PMF between two charged alumina NPs, the charge distribution of the smallest NP (R = 0.85 nm) was altered from the classical CLAYFF force field, which assumes a net surface charge equal to zero. In particular, the positive charges of some surface aluminium atoms were randomly turned off, resulting in a globally negative NP, with a surface charge density, σ_q of -0.346 C/m^2. A more rigorous procedure, including the use of a reactive force field (ReaxFF)[S12] could have also been implemented to tune σ_q of the NP in response to changes in the solution pH. However, the simpler strategy adopted here was deemed adequate in order to demonstrate the sensitivity of the PMF to the NP surface chemical and physical properties.

Atom	σ [nm]	ε [kJ/mol]	q [e]
Bulk Al	0.427	$0.5566 \cdot 10^{-5}$	0
Bulk O	0.3166	0.65020	0
Hydroxyl O	0.3166	0.65020	-0.95
Hydroxyl H	0.0	0.0	0.425
Surface Al (1 bonded OH)	0.427	$0.5566 \cdot 10^{-5}$	0.525
Surface Al (2 bonded OH)	0.427	$0.5566 \cdot 10^{-5}$	1.05
Surface Al (1 bonded OH)	0.427	$0.5566 \cdot 10^{-5}$	1.575

Table S1: Lennard-Jones parameters and partial charge distribution on α-Al_2O_3 [S11]. According to the number of hydroxyl groups bonded to one surface aluminium atom, the Al partial charge is set to q_{Al}= +0.525e for one OH group, q_{Al} = +1.05e for two OH groups, and q_{Al} = +1.575e for three OH groups.

1.1 Convergence of MD Self-Assembly Simulations of Surfactants on Alumina NP

To validate the convergence of sodium dodecyl sulfate (SDS) and dodecyl trimethyl ammonium bromide (DTAB) self-assembly simulations on alumina bare nanoparticles (BNP), we studied the time evolution of the radial distribution function, g(r), of these surfactants wrapping the BNP surface. Specifically, we computed the g(r) of SDS and DTAB residues, using the center of mass positions of both surfactant heads and tails, around the center of mass of the alumina BNP, over various time intervals, during the first 50 ns of MD simulations. Fig. S2 (a) and (b) show the g(r)s of SDS and DTAB residues respectively, after 1 ns, 5 ns, 20 ns, 30 ns, 45 ns and 50 ns. The figures clearly demonstrate that the rearrangement of surfactants on alumina surface tends to stabilize after 20 ns, thereby confirming that the selected timescale is adequate to describe the rearrangement of surfactants on the alumina BNP. Moreover, the g(r)s in Fig. S2 (a) and (b) highlight the conformation of surfactants adsorbed on the alumina NP surface: the hydrophobic tails of both SDS and DTAB tend to distribute closely to the alumina NP, showing peaks at D = 2.24 nm and D = 2.25 nm respectively, while the charged heads project outwards from the alumina surface due to their tendency to be solvated by water (see the second peaks in Fig. S2 (a) and (b)).

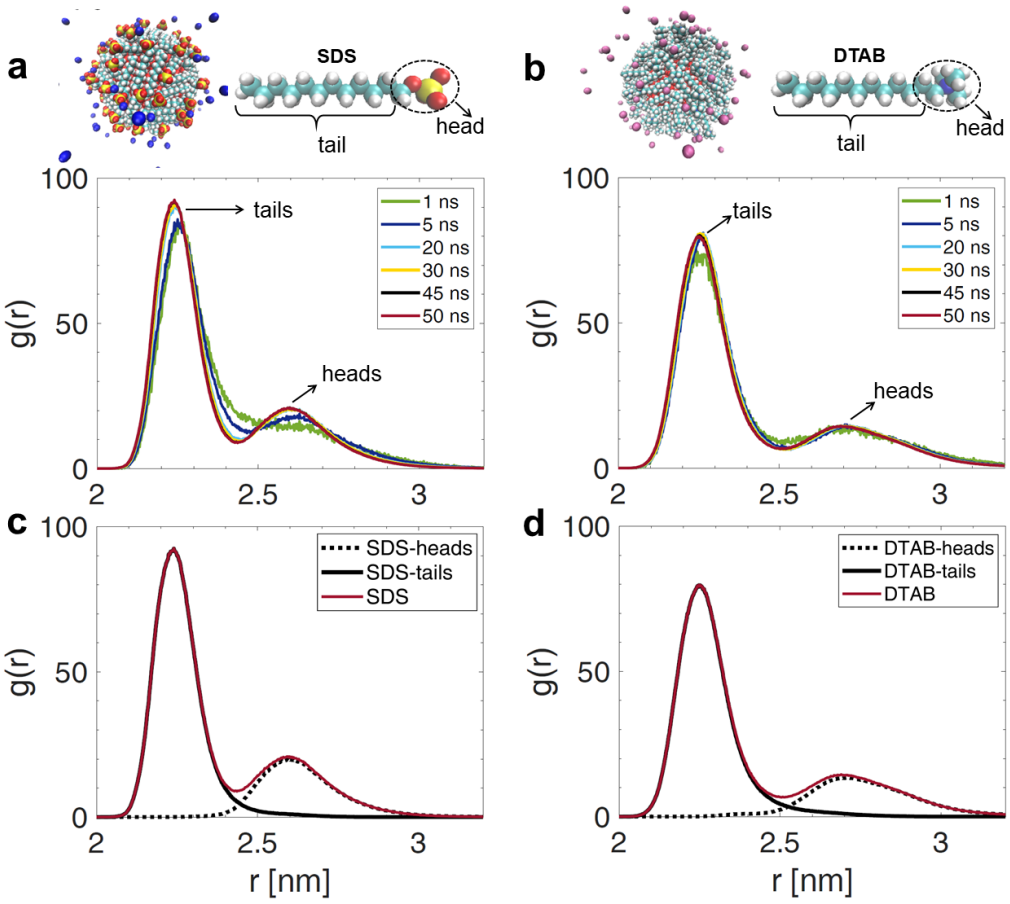

Fig. S2: (a-b) Time evolution of the radial distribution functions (g(r)s) of SDS (a) and DTAB (b) residues around the center of mass (com) of the alumina bare nanoparticle (BNP). (c-d) The SDS and DTAB g(r)s (red curves) are compared at t = 50 ns with the radial distribution functions obtained by considering separately the com positions of the tails and the heads of the SDS (c) and DTAB (d) molecules around the com of BNP. Note that all the computed g(r)s are normalized with respect to the total number of residues, namely tails and heads, present in the system.

In Fig. S2 (c) and (d), we demonstrate that the radial distribution functions, (g(r)s), corresponding to the total SDS and DTAB residues (red curves in Fig. S2 (c) and (d)) can be derived by considering separately the radial distribution of the com positions of surfactant heads ($g_{head}(r)$) and tails ($g_{tail}(r)$), namely: $g(r) = g_{head}(r) + g_{tail}(r)$. Note that all the computed g(r)s are normalized over the total number of surfactant residues, both heads and tails wrapping each CNPs.

Finally, the radial distribution functions of SDS and DTAB residues around the bare nanoparticles (see Figure 1(d) in the main text) were also used to estimate the radius, R_{CNP}, of SDS and DTAB CNPs. Precisely, $\mathrm{R_{CNP}} = \sum(\mathrm{g(r)} \cdot \mathrm{r})/\sum \mathrm{g(r)} + \mathrm{r_a}$, where $\mathrm{r_a} = 0.05\ \mathrm{nm}$ is mean atomic radius. Through this equation, we obtained $\mathrm{R_{SDS-CNP}} = 2.41\ \mathrm{nm}$ and $\mathrm{R_{DTAB-CNP}} = 2.45\ \mathrm{nm}$.

2. Potential of Mean Force (PMF) Calculations

Fig. S3 illustrates the results of the PMF between uncharged BNPs in vacuum. The mean forces, plotted in Fig. S3 (a) as a function of the center of mass distance, D, show the short-range behavior

of the interactions. This result allowed us to detect the interaction potential range and to select the most significant D values, namely, from 3.9 nm to 5 nm, used in the PMF simulations. The PMF in vacuum was evaluated for frozen and vibrating BNPs, and the two cases are shown in Fig. S3 (b) with blue and green symbols, respectively. An examination of Fig. S3 (b) shows that the largest deviation between the two curves, ΔPMF = 7.5 kJ/mol, occurs at D = 4.1 nm, and is around 18% of the PMF. This small difference reinforces the use of frozen NPs to fix the center of mass distance during the course of the simulation.

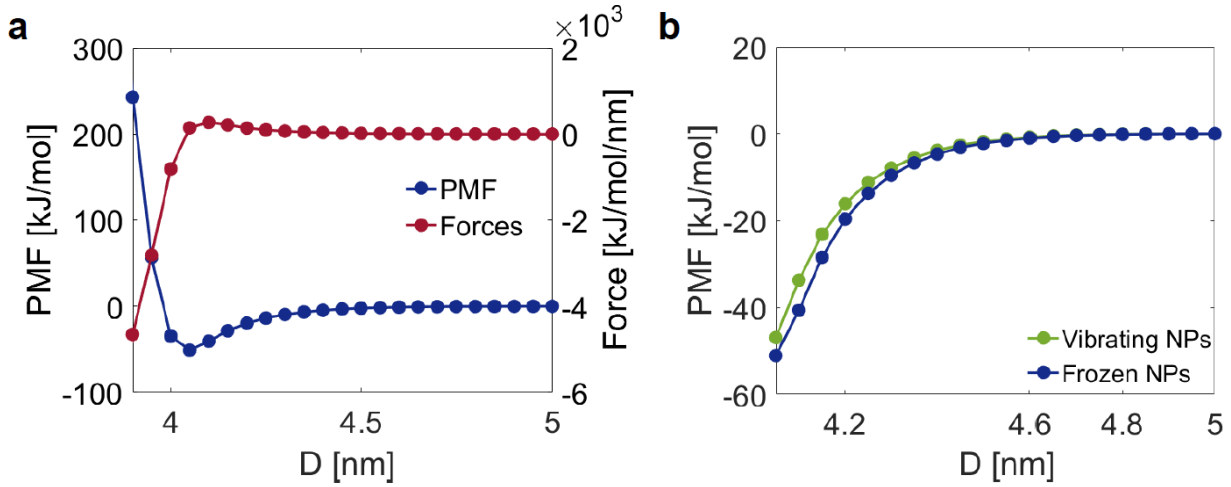

Fig. S3: (a) Mean forces and potential of mean force (PMF) obtained from MD simulations between two frozen BNPs in vacuum as a function of the center of mass distance, D. Note that –Forces (D), instead of +Forces (D), are plotted to improve the clarity of the plot. (b) Comparison of the PMFs for frozen and vibrating BNPs.

A sensitivity analysis was carried out to qualitatively investigate the effects of surface charges and salt concentration on the PMF. To evaluate the PMF between two charged alumina NPs, the simulation protocol of 'pulling' was adopted. Specifically, two NPs are placed in a box (22 nm x 8 nm x 8 nm) made of SPC/E water molecules[S13]. It is worth noting that 44 molecules of water were replaced by an equal number of positive counterions (Na^{+1}) to ensure electroneutrality of the simulated system. A similar approach was followed when a salt concentration of [NaCl] = 0.01 M was added to the bulk aqueous solution. After the energy minimization, the entire system was equilibrated at T = 300 K in the Canonical ensemble (NVT), by applying the Nosé-Hoover thermostat[S14]. The second equilibration step was carried out in the isothermal-isobaric ensemble (NPT, T = 300 K and 1 bar), using the Parrinello-Rahman barostat[S15]. First, the distance between the NPs centers of mass was set to 2 nm. Then, by restraining one NP (reference group) while pulling the second one (pull group) along a reaction coordinate, D, a series of windows, corresponding to different inter-NP separation distances, are generated as shown in Fig. S4 (a). Specifically, the pull velocity is kept constant (v_{pull} = 0.01 nm/ps) to allow a linear uniform motion of the pulled NP. From the resulting trajectories, the snapshots generated from independent 2 ns MD simulations have an inter-window spacing equal to 0.25 nm, which is a trade-off distance ensuring good precision and affordable processing time. During the simulations, the center of mass positions of the NPs are maintained fixed by the SHAKE algorithm implemented in GROMACS. Before running the actual MD simulations, each window is briefly equilibrated in the NPT ensemble for 200 ps. The PMF is finally

calculated by numerically integrating the inter-NP forces obtained in each space-window, as reported in the main text.

The results of the simulated PMF are shown by the red dots in Fig. S4 (b). The MD simulations data were fitted by Eq. 2 (Case 1) and the fitting function is represented by the red solid curve. Unlike the neutral NPs, the PMF between two charged NPs exhibits a long-range repulsive potential, which extends from D = 2.24 nm to D = 8 nm, with a maximum of around 98 kJ/mol at D = 2.24 nm (Fig. S4 (b)). When the NPs approach each other closer than 2.24 nm, the repulsive interaction is slightly weakened by the short-range dispersion potential (PMF = 68 kJ/mol at D = 1.98 nm).

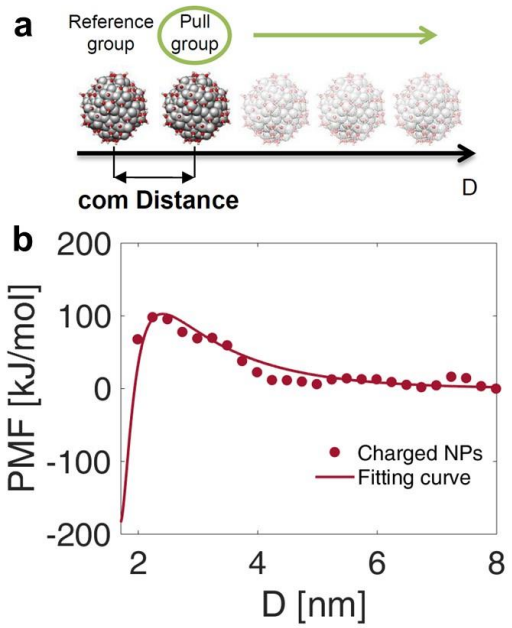

Fig. S4: (a) Pulling procedure to generate the simulated configurations for two alumina NPs of 0.85nm radius, located at different center of mass distances (D). (b) Simulated PMF corresponding to two charged NPs in aqueous solution (red dots). The fitting of the PMF data corresponds to the solid red line.

In order to fit the primary features of the PMF vs. D curve, we used the following empirical expression:

$$\mathrm{PMF(D)} = \mathrm{a}\left(\frac{1}{(\mathrm{D}-\mathrm{x_0})}\right)^{\mathrm{n}} - \mathrm{b}\left(\frac{1}{(\mathrm{D}-\mathrm{x_0})}\right)^{\mathrm{m}} + \sum_{\mathrm{i}=1}^{2} \mathrm{c_i}\cdot\exp\left(-\frac{(\mathrm{D}-\mathrm{x_1})}{\lambda_\mathrm{i}}\right) \qquad (2)$$

The various terms in Eq. 2 aim to reproduce both the repulsive and the attractive interactions as a function of D when two NPs approach each other. Specifically, the first term describes the sharp repulsion due to excluded-volume effects; the second term reflects the attractive interactions, and the last two terms (i = 1 and 2) reflect the repulsive effects of entropic nature. The ten parameters (a, n, b, m, c_1, c_2, λ_1, λ_2, x_0, x_1) in Eq. 2 were obtained using a least-square fitting approach, and they are reported in Table S2.

	$\mathrm{a}\left[\frac{\mathrm{kJnm^n}}{\mathrm{mol}}\right]$	n	$\mathrm{b}\left[\frac{\mathrm{kJnm^m}}{\mathrm{mol}}\right]$	m	$\mathrm{c_1}\left[\frac{\mathrm{kJ}}{\mathrm{mol}}\right]$	$\mathrm{c_2}\left[\frac{\mathrm{kJ}}{\mathrm{mol}}\right]$	$\lambda_1[\mathrm{nm}]$	$\lambda_2[\mathrm{nm}]$	$\mathrm{x_0[nm]}$	$\mathrm{x_1[nm]}$

Case1	$1.5 \cdot 10^7$	20.0	$1.55 \cdot 10^5$	10	23.6	191	1.606	1.3	0.0	1.7
Case2	1.0774	7	1.2134	5	422.28	0.0	0.3	0.0	3.34	3.9
Case3	0.0	0.0	0.0	0.0	235.3	0.0	0.7133	0.0	0.0	4.9
Case4	0.6480	7	13.25	1.0	326.7	0.0	0.9	0.0	4.78	4.7

Table S2: Compilation of the ten fitted parameters in Eq. 2. Note that Case 1, Case 2, Case 3, and Case 4 correspond to charged BNPs of R = 0.85 nm and [NaCl] = 0.01 M, neutral BNPs of R = 2 nm, DTAB CNPs of R = 2.45 nm, and SDS CNPs of R = 2.41 nm.

2.1 Convergence of the PMF Calculation for DTAB Coated NPs

The Potential of Mean Force (PMF) of the Coated NPs (CNPs) was carried out at various center of mass separation distances (D), from 4.9 nm to 8 nm, thereby creating 31 configurations. In each configuration, the PMF was calculated after having obtained 10-ns long trajectories, including 4 ns of equilibration and 6 ns of actual production run. The resulting forces are then collected in the last 2 ns of the trajectories. We note that during the calculation of the PMF, we froze only the core of the alumina nanoparticles (NPs), while allowing the surfactant anions to randomly move around the bare NPs. This calculation has allowed us to explore multiple configurations and mutual orientations of the surfactant anions, during the complete molecular dynamics (MD) trajectory used for the PMF analysis. As the Fig. S5 shows, the mutual orientation of the coated NPs, in the z direction, does not remain fixed even within 1 ns.

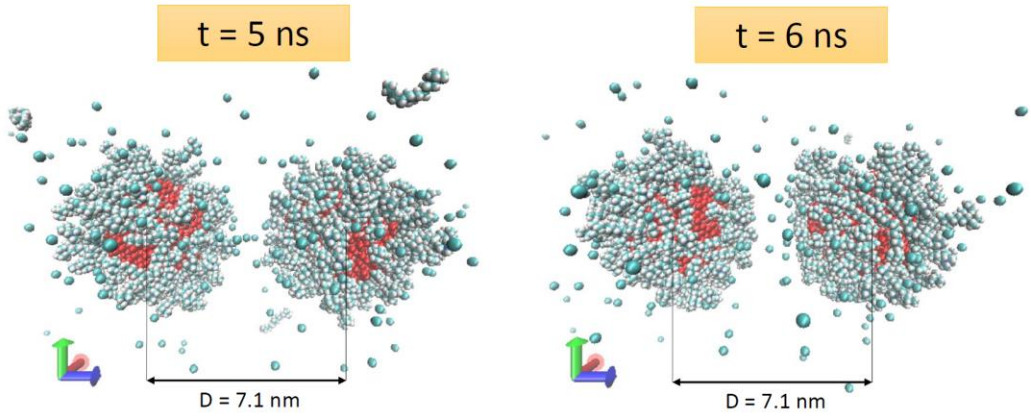

Fig. S5: Molecular Dynamics snapshots showing the mutual orientation of two DTAB coated NPs after 5 ns (left-hand side) and 6 ns (right-hand side) of production run. Because of the random motion of the surfactants, the CNPs continuously change their configuration during the simulation time, thereby exhibiting several mutual orientations.

Note that during the 6 ns of production run, all the PMF windows corresponding to the 31 CNP separation distances preserve the configurations with the surfactants wrapping the NPs and completely adsorbed to the bare alumina surface (see Figure 2 (b) and (c) of the main manuscript). However, at very short separation distances, the constrained and the energy unfavourable positions of the CNPs (see the PMF profiles in Figure 2 of the main manuscript) may influence the rearrangement of surfactants after 6 ns of production run. Such possible reorganization of

surfactant molecules after 6 ns has not been considered for the PMF calculation because it may not be representative of the actual behaviour of CNPs in a real nano-suspension.

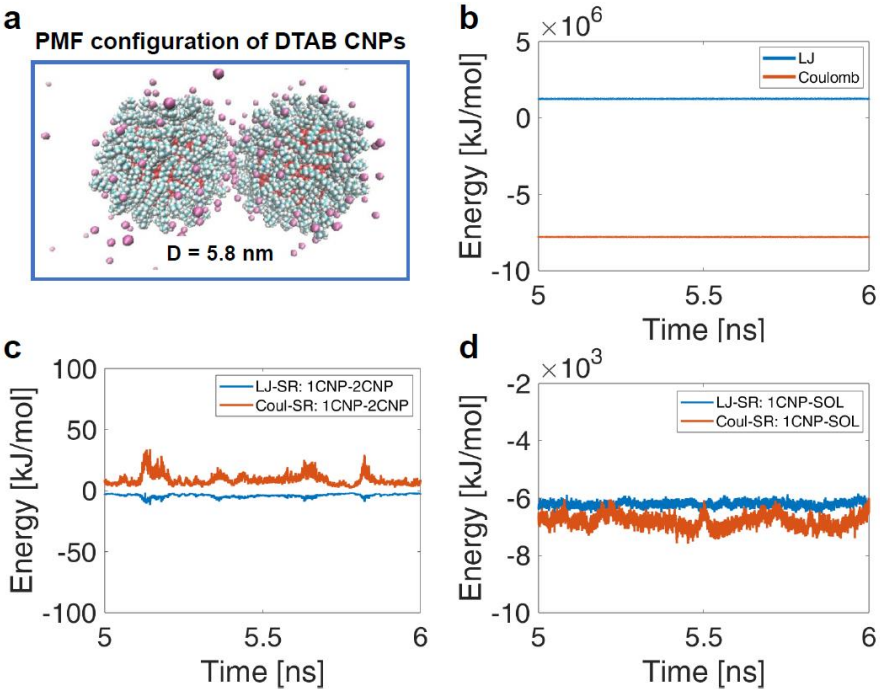

Fig. S6: (a) Representative PMF simulation snapshots of two DTAB CNPs in the xz plane obtained for D = 5.8 nm. (b) Total Lennard-Jones (LJ) and Coulomb interactions corresponding to the whole solvated configuration shown in (a). Note that both short and long range interactions are included in the calculation of LJ and Coulomb energies. (c) Lennard-Jones (LJ) and Coulomb (Coul) short range (SR) interactions between the DTAB CNPs shown in (a). (d) Lennard-Jones (LJ) and Coulomb (Coul) short range (SR) interactions between one single DTAB CNP and the surrounding water molecules.

In order to check the convergence of MD simulations within the 6 ns of production run, we calculated, according to the Eq. 1, the Lennard-Jones (LJ) and Coulomb interaction energies during the last 1 ns of the MD production run. As an exemplificative study case, we considered the configuration of two solvated DTAB CNPs when their separation distance, D, is 5.8 nm (see the snapshot in Fig. S6 (a)). In Fig. S6 (b), the total Lennard-Jones and Coulomb interactions are shown. Here, both short and long-range interactions are considered. Moreover, all the contributions coming from water molecules, surfactants, ions and alumina atoms are included in the calculation of Lennard-Jones and Coulomb energies. In Fig. S6 (c), we restricted the calculation to the short-range (SR) LJ and Coulomb energies between the DTAB CNPs shown in Fig. S6 (a), while in Fig. S6 (d), the previous mentioned non bond interactions are calculated between one single DTAB CNP and the water molecules (SOL). All the energies computed and shown in Fig. S6 highlight the steady-state behaviour of the MD simulations, thereby confirming that the chosen time scale for the PMF calculation is reasonable. Note that in the current analysis, we concentrated on a few pair-wise potential combinations, namely between CNPs and water molecules, however, the effective mean

force utilized to compute the PMF is the result of all possible coupled effects, including the entropic contribution between each single molecule in the system.

3. Classical DLVO and Extended DLVO Theories

The classical DLVO theory, which currently represents the cornerstone underlying our understanding of the interactions between colloidal particles, including their aggregation behavior, was developed by Derjaguin, Landau, Vervey, and Overbeek (DLVO)[S18,S19]. According to the DLVO theory, the inter-particle energy between suspended NPs depends on the additive contributions of both van der Waals and electrostatic interactions, which depend on the interparticle distance. The classical DLVO parameters corresponding to the study cases discussed in the main text are reported in Table S3.

NP	$\mathbf{R}\,[\mathbf{nm}]$	$\boldsymbol{\sigma_q}\left[\frac{\mathbf{C}}{\mathbf{m^2}}\right]$	[NaCl] [M]	$\boldsymbol{\rho_{bulk}}\left[\frac{\#}{\mathbf{m^3}}\right]$	$\boldsymbol{\rho_{ci}}\left[\frac{\#}{\mathbf{m^3}}\right]$	$\boldsymbol{\lambda_d}[\mathbf{nm}]$	$\boldsymbol{\psi_0}[\mathbf{V}]$
Charged BNP	0.85	-0.346	0.01	$6.022\cdot10^{24}$	$3.14\cdot10^{25}$	1.606	-0.211
Neutral BNP	2	0.0	0.0	0.0	0.0	0.0	0.0
SDS CNP	2.41	-0.184	0.0	0.0	$5.83\cdot10^{25}$	1.386	-0.120
DTAB CNP	2.45	+0.212	0.0	0.0	$6.95\cdot10^{25}$	1.269	0.122

Table S3: Input parameters for the classical DLVO theory for the study cases discussed in the main text. R is NP radius, σ_q is the surface charge density, [NaCl] is the salt concentration, ρ_{bulk} is the number density of the salt in the bulk solution, ρ_{ci} is the number density of counterions, λ_d is the Debye-Hückel screening length and ψ_0 the surface electrical potential.

In Fig. S7, a comparison of the simulated PMF for two charged BNPs (red dots) with some of the well-known formulations of the classical DLVO potentials (coloured continuum curves) is reported. Specifically, we obtained the DLVO interaction potentials as a summation of the nonretarded van der Waals contribution ($U_{vdw}(D)$ reported in the Eq. 2 of the main text) and the Electric Double Layer ($U_{EDL}(D)$) interactions. Four different formulations of $U_{EDL}(D)$ has been utilized: (i) the Linearized Poisson Boltzmann (DLVO-LPB, blue line in Fig. S7)[S20], (ii) the Non-Linearized Poisson Boltzmann (DLVO-NLPB, orange line in Fig. S7)[S21], (iii) the Hogg-Healy-Fuersteneau (DLVO-HHF, orange line in Fig. S7)[S22], and (iv) the modified Hogg-Healy-Fuersteneau (DLVO-HHF, yellow line in Fig. S7)[S21].

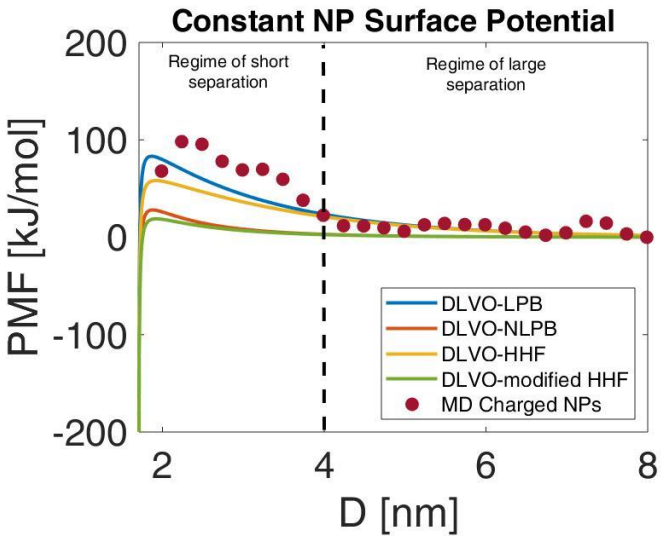

Fig. S7: Simulated PMF corresponding to two charged NPs in aqueous solution (red dots). The classical DLVO theory prediction (obtained as DLVO = $U_{vdw}(D) + U_{EDL}(D)$ is computed following four different formulations of $U_{EDL}(D)$: the Linearized Poisson Boltzmann (DLVO-LPB in Eq. 3), the Non Linearized Poisson Boltzmann (DLVO-NLPB in Eq. 4), the Hogg-Healy-Fuersteneau (DLVO-HHF in Eq. 5), the modified Hogg-Healy-Fuersteneau (DLVO-modified HHF in Eq. 6).

The following equations (3-6) correspond to the previous mentioned DLVO formulations (i-iv), respectively:

$$\mathrm{DLVO-LPB(D)} = \mathrm{Uvdw(D)} + 2\pi R\varepsilon_0\varepsilon_r{\psi_0}^2 e^{-\kappa(D-2R)}, \tag{3}$$

$$\mathrm{DLVO-NLPB(D)} = \mathrm{Uvdw(D)} + 4\pi\varepsilon_0\varepsilon_r Y(D)^2\left(\frac{k_B T}{e}\right)^2\frac{R^2}{D}e^{-\kappa(D-2R)}, \tag{4}$$

$$\mathrm{DLVO-HHF(D)} = \mathrm{Uvdw(D)} + \pi R\varepsilon_0\varepsilon_r{\psi_0}^2\log\left(\frac{1+e^{-\kappa(D-2R)}}{1-e^{-\kappa(D-2R)}}\right) + \log(1+e^{-\kappa(D-2R)}), \tag{5}$$

$$\mathrm{DLVO-modifiedHHF(D)} = \mathrm{Uvdw(D)} + 4\pi\varepsilon_0\varepsilon_r Y(D)^2\left(\frac{k_B T}{e}\right)^2\frac{R^2}{D}\log(1+e^{-\kappa(D-2R)}), \tag{6}$$

where k_B is the Boltzmann constant, T is the absolute temperature, ε_0 and ε_r are the dielectric permittivity of vacuum and water, respectively, κ is the inverse of the Debye-Hückel screening length ($\kappa = 1/\lambda_d = \sqrt{(\sum \rho_i (ze)^2)/(\varepsilon_0\varepsilon_r k_B T)}$), and *e* is the electronic charge. The function Y in Eq. 4 and Eq. 6 is given by[S21]:

$$Y(D) = \frac{4\exp(-\kappa(D-2R)/2)}{\tanh\left[\exp(-\kappa(D-2R)/2)\cdot\tanh\left(\frac{ze\psi_0}{4k_B T}\right)\right]}, \tag{7}$$

where ψ_0 is the surface potential and is obtained after solving the Grahame equation[S20]. All the input parameters used in the Eq. (3-6) are provided in Table S3. Note that Eqs. 3 and 5 are obtained under the approximation of low surface particle potential, ψ_0, whereas Eqs. 4 and 6 are expected to be accurate from moderate to high surface potential, and for this reason they are more suitable to describe the interactions of the highly charged BNP here investigated. Specifically, Eq. 6 is derived

for modest to large κR and for all separation κ(D-2R), therefore it is the classical DLVO formulation closest to the analysed case. As Fig. S7 highlights, for D > 4 nm, the simulated PMF agrees quite well with the classical DLVO theories (Eqs. 3-6). However, while the DLVO correctly describes the interaction potential in the far-field continuum aqueous media region, it strongly deviates from the simulated PMF for 2 nm < D < 4 nm. As already pointed out in the main text, one of the reasons for the mismatch between the DLVO theory and the MD simulations is related to the ion-ion correlations effects, the modification of the dielectric constant, and the hydration repulsion acting at the solid-liquid interface[S16,S17]. Moreover, in the short-range interaction regime, the linear superposition approximation utilized to derive the DLVO fail. At D = 2.24 nm, the simulated PMF exceeds the DLVO theory prediction by around 80 kJ/mol (see Fig. S7).

A large body of literature shows that the classical DLVO theory reveals a pronounced inaccuracy to describe highly charged and coated particle interactions in the short-rang NP separation regime. Hereafter, we present two examples of modified classical DLVO theory. Specifically, we apply the charge renormalization theory and the polymer grafted theory to evaluate the interaction energy between highly charged and coated NPs respectively.

3.1 Beyond Classical DLVO: The Charge Renormalization Theory

In the field of highly charged colloidal suspensions, the concept of effective or renormalized surface charge plays a significant role to describe the inter-particle interaction potentials[S23,S24]. In such suspensions, the strong electrostatic forces induced by the charged colloids bring to the formation of a condensed shell of counterions in the vicinity of NP surface, while a diffuse layer of co-ions and counterions is forming the far-field aqueous media region. The basic idea of the charge renormalization theory is to consider the structural NP and its condensed counterions as a whole which carries an effective charge, Z_{eff}, much weaker than the structural one, Z_{str}. Consequently, the non-linear behaviour induced by the charged NP with Z_{str} can be embodied in a linear screening model computed by utilizing the renormalized effective charge Z_{eff}. In order to compare the simulated PMF with a predictive theoretical potential based on the charge renormalization theory, we restricted the analysis to the case of very dilute NP suspensions[S23]. In fact, several studies, by applying the Wigner Seitz (WS) cell model, have extended the renormalization charge theory to the case of very concentrated suspensions[S24,S25] . However, the NP concentrations, Φ, examined in this paper (0.00125 < Φ < 0.05) fall down to the case of dilute suspensions (Radius of the WS cell, $R_{WC} = R(\frac{4}{3}\pi R^3\Phi)^{-1/3} \to \infty$)[S25]. In Fig. S8, the simulated PMF (red dots) are compared with the DLVO interaction potentials (coloured continuum curves) calculated at constant NP effective charges, Z_{eff}, after having considered the Linearized Poisson Boltzmann (LPB) theory for the EDL interaction, namely[S23]:

$$\mathrm{DLVO} = \mathrm{Uvdw(D)} + \frac{{Z_{eff}}^2(k_B T)L_B(\exp(\kappa R))^2}{(1+\kappa R)^2}\frac{e^{-\kappa(D-2R)}}{D}, \quad (8)$$

where $L_B = e^2/(4\pi\varepsilon_0\varepsilon_r k_B T)$ is the Bjerrum length, κ the inverse of the Debye-Hückel screening length, R the NP radius. A sensitivity analysis was carried out by tuning the effective charge, Z_{eff},

from the actual structural surface charge Z_{str} = 22 *e* to Z_{eff} = 3.76 *e* corresponding to the theoretical value in the limit of low salinity, $\kappa R << 1$, namely[S23]:

$$\frac{zZ_{eff}L_B}{R} = 2\log\left(\frac{1}{\kappa R}\right) + 2\log\left(\log\left(\frac{1}{\kappa R}\right)\right) + 4\log(2), \quad (9)$$

where z is the ion valence. As Fig. S8 shows, the interaction potentials evaluated according to the renormalization of charge theory agree quite well in the regime of large separation between the two charged NPs, however, they deviate in the short range of interactions, where effects associated with solvation forces and nonzero counterion/co-ion sizes are important. Although an adjustable Z_{eff} could be selected to fit the MD results for D > 2.5 nm, the resulting theoretical energy barrier would largely overestimate the simulated PMF for D < 2.5 nm.

Note that Monte Carlo simulations and Molecular Dynamics have been relatively successful to evaluate the effective surface charge Z_{eff}[S25,S27], however, our attempt in this study was to compare the simulated PMF with a self-consist theoretical approach able to calculate analytically the effective renormalized charge Z_{eff}.

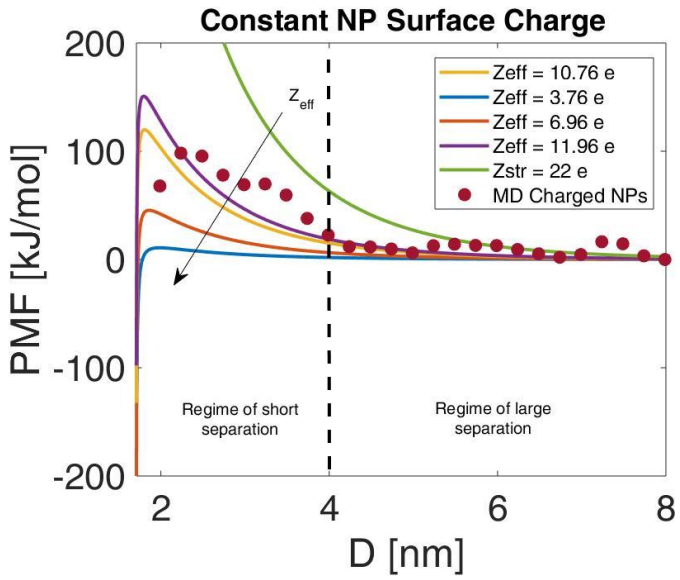

Fig. S8: Simulated PMF corresponding to two charged NPs in aqueous solution (red dots). The coloured continuum lines correspond to the DLVO interaction potential at constant NP surface charge after considering the Linearized Poisson Boltzmann (LPB) theory with renormalized effective surface charges, Z_{eff}, in the limit of very dilute NP suspensions (Eq. 8). For comparison, the DLVO interaction potential is also computed utilizing the LPB approximation with the structural surface charge, Z_{str}, in the limit of dilute suspensions.

3.2 Extended DLVO for Coated NP Interactions

Here, we present an example of the extended DLVO theory as implemented for DTAB CNPs. Specifically, we considered the following semi-empirical equation, widely used for polymer-grafted surfaces, which aims to describe the entropic repulsive contribution[S28].

$$\mathrm{U_{exDLVO}(D)} = 32\mathrm{RL^2\Gamma^{\frac{3}{2}}k_BT}\cdot\exp\left(-\frac{(\mathrm{D}-2\mathrm{R})}{\mathrm{L}}\right) \quad (10)$$

where R = 2.45 nm is the radius of the CNP, L = 0.89 nm is the protrusion length of the surfactant tails, and Γ = 1.99 nm^{-2} is the number of surfactant chains (tails) per unit area. Accordingly, the final continuum theory used to describe the interaction potential between two NPs is given by:

$$\mathrm{U_{CNP}(D)} = \mathrm{U_{vdw}(D)} + \mathrm{U_{EDL}(D)} + \mathrm{U_{exDLVO}(D)}, \quad (11)$$

where $U_{vdw}(D)$ and $U_{EDL}(D)$ are detailed in the Methods section of the main text (Eqs. 2 and 4 in the main text), with the corresponding parameters reported in Table S3, and $U_{exDLVO}(D)$ is calculated using Eq. 10. The resulting potential profile ($U_{CNP}(D)$) is shown by the black dotted curve in Fig. S9, and clearly shows the limitation of the extended DLVO theory when compared to the simulated PMF vs. D profile (the yellow dots and fitted yellow curve in Fig. S9). For D > 5.4 nm, the extended DLVO profile is closer to the simulated PMF than is the classical DLVO theory (the black solid curve in Fig. S9). However, $U_{CNP}(D)$ strongly overestimates the PMF values for D < 5.4 nm. Therefore, from the above analysis, we conclude that any combination of continuum models would fail to adequately incorporate the coupled and discrete effects occurring at the nanoscale and affecting the actual interactions between NPs when they are closer than 1 nm.

In order to utilize our computational resources efficiently, the PMF in the region D < 4.9 nm was not simulated. In fact, the aggregation kinetics of the NPs is primarily governed by the primary free energy barrier which has been considered in case of DTAB CNPs as the maximum value of the PMF corresponding to the smallest NP separation distance. Such value of PMF, located at Db = 4.9 nm, plays a dominant role in modulating the rate of aggregation of the CNPs. Because the primary free energy barrier is quite high, the probability that two CNPs overcome it, and aggregate as a result, is extremely low. Therefore, for D values smaller than Db, the PMF should not affect the kinetics of NP aggregation, and for this reason, was not computed. Nevertheless, the trend exhibited by the PMF for D < 4.9 nm can be deduced from a previous study by Xu *et al*., who computed the PMF of SDS coated SWCNTs[S29]. Further, the different slopes of the PMF curves corresponding to the SDS and DTAB CNPs when D < 5.2 nm reflect the different magnitudes of the forces acting between the coated NPs.

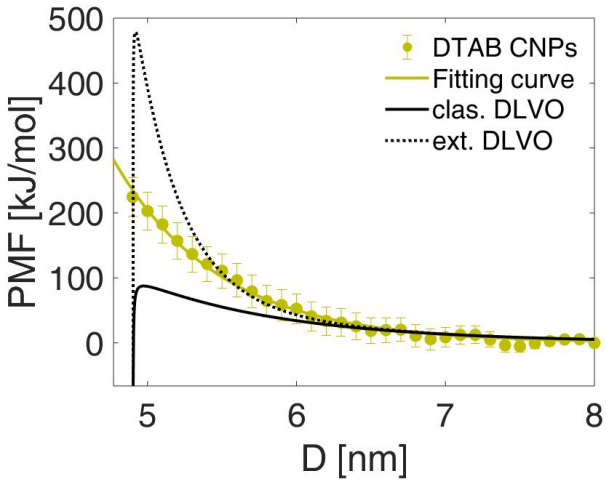

Fig. S9: PMF of DTAB CNPs vs. D and comparison with the DLVO theory: Simulated PMF between two interacting DTAB CNPs (yellow dots). The fitting curve to the simulated PMF data is obtained using Eq. 2, and it is shown by the solid yellow curve. The interaction potential energies predicted by the classical (the solid black curve) and the extended DLVO theory (the dashed black curve) are shown for comparison.

In the previous examples, we have shown that even the most elegant adaptations of the classical DLVO fail to describe the NP-NP interaction in the short-range regime. Consequently, mean-field theories like the Poisson-Boltzmann model which consider charged species like counterions to be point-sized are unable to properly describe the electric double layer effects. Similarly, the assumptions of uniform and continuous media, underlying the DLVO theory, break down in the proximity of the NP surface, where an interfacial layer of highly structured water occupies a region whose thickness is not negligible relative to the NP dimensions. Moreover, coupled effects may arise in such nanoscopic systems, and the hypothesis that the inter-particle potential is a superposition of independent interactions could be violated.

4. Stochastic Dynamics Simulations

4.1. Convergence of the Simulations

The kinetics of NP aggregation was simulated by implementing the Langevin equation[S30]:

$$m_i \frac{d^2\mathbf{r}_i}{dt^2} = -m_i\gamma_i \frac{d\mathbf{r}_i}{dt} + \mathbf{F}_i(\mathbf{r}_i(t)) + \sqrt{2m_i\gamma_i k_B T}\,\mathbf{r}_i^{G}, \quad (12)$$

where m_i is the mass of NP_i, $\mathbf{r}_i$ is its position at time t, k_B is the Boltzmann constant, T is the absolute temperature, $\mathbf{r}_i^G$ is the Gaussian distributed noise, and γ_i is the friction coefficient associated with the stochastic collisions of the nanoparticle, NP_i, with the molecules constituting the solvent. It is worth noting that in the limit of high friction, i.e. in over-damped systems where the inertia term is negligible, Eq. 12 reduces to the equation of Brownian dynamics. For the sake of completeness in this study we solved the complete Langevin equation, avoiding any assumption about the inertia effects. To derive the force $\mathbf{F}_i$ associated with particle *i* using Eq. 12, we developed an inter-particle

potential based on the previously discussed atomistic PMFs. The friction coefficients, γ, were obtained using the Stoke's relation[S31], and the values for the various cases considered are summarized in Table S3 .

Table S4: Friction coefficients, γ, used in the stochastic dynamics simulations of suspended NPs in aqueous media. Note that $\gamma = 6\pi\mu R$, where μ is the water viscosity and R is the NP radius.

NPs	Radius [nm]	$\gamma \cdot 10^{-11}$ [kg/s]
Charged BNP	0.85	1.363
Neutral BNP	2	3.207
SDS CNP	2.41	3.864
DTAB CNP	2.45	3.929

It is worth noting that the CNPs are treated as Brownian particles having an equivalent radius equal to the radius of the BNP plus the thickness of the surfactant coating in the NP. A thicker coating is attributed to the DTAB NPs because of their morphology, as discussed in the Results and Discussion section. Some representative snapshots of the SD simulations are shown in Fig. S10. Specifically, in Fig. S10 (a) and (b) we qualitatively compare the cluster distribution in a NP suspension of volume fraction Φ = 1% when the classical DLVO (Eq. 2 in the main text) theory and the calculated PMFs (Case2 in Table S2) are used respectively as inter-particle potentials. As already discussed, the potential energy predicted by the DLVO theory between two BNPs overestimates the attractive interaction energy, thereby leading to a fast kinetics of NP aggregation. Fig. S10 (c) shows an example of a fully aggregated nano-suspension with volume fraction Φ = 5%.

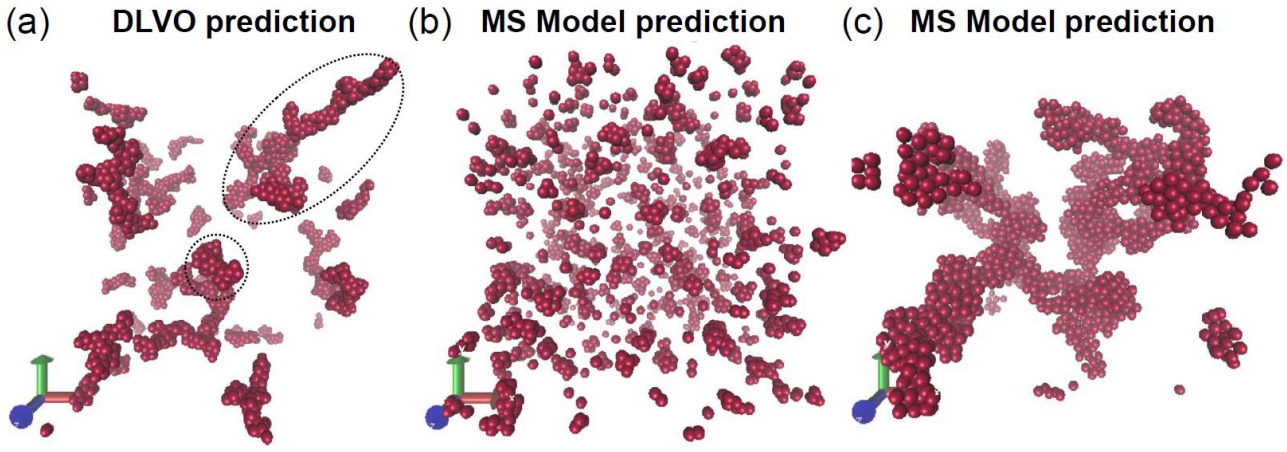

Fig. S10: (a-b) Representative SD simulation snapshots of a NP suspension with Φ = 1% at t = 0.1 ms obtained by assuming (a) the DLVO theory, and (b) the simulated PMF as the NP interaction potential energy. Both compact and elongated clusters are highlighted in (a), contrary to the standard assumptions in the DLCA regime about cluster shape and size. (c) SD simulation snapshot of a NP suspension with Φ = 5% obtained by implementing the current Multi-Scale (MS) model. About a single cluster is observed.

The convergence of the SD simulations was evaluated by monitoring the evolution of the total energy in time. Fig. S11 (a) and Fig. S11 (b) show the sum of the potential and the kinetic energies

of the nano-suspensions considered as a function of the simulated time. We report the evolution of the total energy for several NP volume fractions in the case of charged BNPs (Fig. S11 (a)) and neutral BNPs (Fig. S11 (b)). While the SD simulations of charged BNP suspensions reach steady state almost immediately (see Fig. S11 (a)), the SD simulations of neutral BNP suspensions attain steady state only after 0.8 ms (see Fig. S11 (b)).

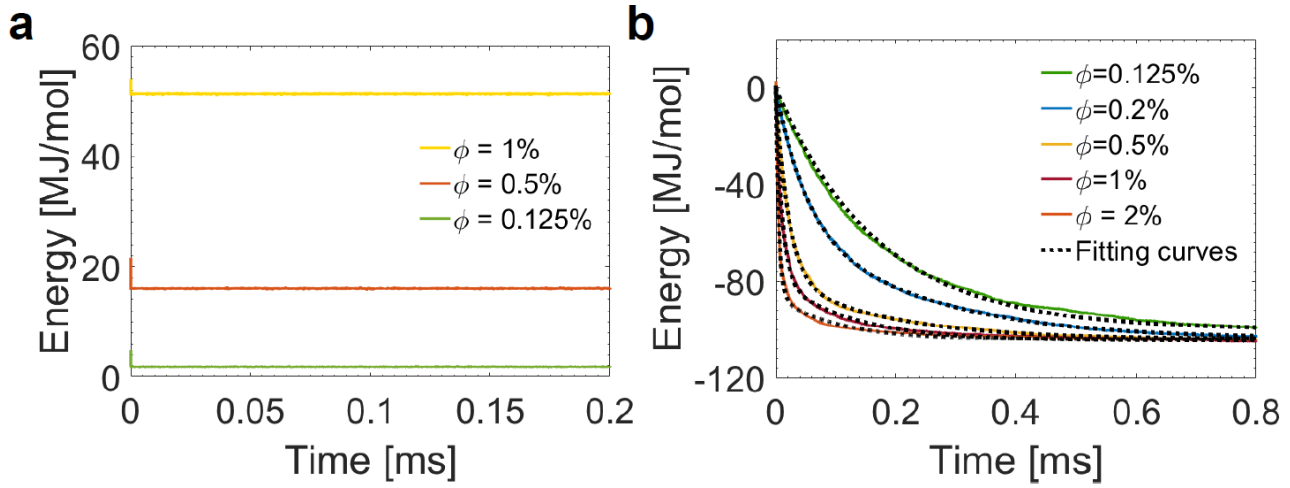

Fig. S11: (a) Total energy vs. time calculated using stochastic dynamics simulations of suspended NPs (R = 0.85 nm, and σ_q = -0.346 C/m^2) in aqueous solution with [NaCl] = 0.01 M. Three particle volume fractions, Φ, are considered. (b) Total energy vs. time calculated using stochastic dynamics simulations of suspended NPs of Radius = 2 nm in aqueous solution. Five particle volume fractions, Φ, are considered.

In order to validate the convergence of the SD simulations, we extrapolated the variation of the total energy after 12 hours from the last step of the SD simulations, namely from 0.8 ms. Specifically, we first fitted the energy vs. time curves shown in Fig. S11 with the following equation:

$$E = -E_0\left(1 - \exp\left(-t/\tau_0\right)\right) + \sum_{i=1}^{2} E_i \exp\left(-t/\tau_i\right), \quad (13)$$

where E_0, τ_0, E_i, and τ_i are the fitting parameters reported in Table S4. Then, we evaluated the percentage variation as follows:

$$var = \frac{(|E_{fin}| - |E_{in}|)/|E_{fin}|}{t_{fin} - t_{in}} \quad (14)$$

where t_{fin} is the final time considered for the calculation, namely 12 hours, E_{fin} is the energy value at t_{fin}, and E_{in} is the value of the total energy at $t_{in} = 0.8$ ms.

Φ [%]	E_0 [MJ/mol]	E_1 [MJ/mol]	E_2 [MJ/mol]	τ_0 [ms]	τ_1 [ms]	τ_2 [ms]	R^2
0.125	100	0	0	$1.698 \cdot 10^{-1}$	-	-	0.996
0.2	103.5	79	-79	$5.91 \cdot 10^{-2}$	$1.792 \cdot 10^{-1}$	$8.94 \cdot 10^{-2}$	0.999
0.5	103.6	79.15	-79.1	$2.34 \cdot 10^{-1}$	$2.1 \cdot 10^{-2}$	$2.558 \cdot 10^{-1}$	0.999
1	104.5	79	-79	$1.124 \cdot 10^{-1}$	$1.04 \cdot 10^{-2}$	$1.096 \cdot 10^{-1}$	0.995

2	104	17.62	-18.82	$5.13 \cdot 10^{-3}$	$9.92 \cdot 10^{-2}$	$4.5 \cdot 10^{-3}$	0.996

Table S4: Compilation of the six fitted parameters in Eq. 13 utilized to reproduce the energy profile as a function of time (see Fig. S11 (b)). Note that the fitting data were found for each volume fraction Φ. R^2 indicates the goodness of the fit.

We found that the percentage variation of the total energy in approximately 12 hours is always less than $6.64 \cdot 10^{-9}$ %. This extremely low value validates the steady state condition of the nano-suspensions considered after 0.8 ms. Note that for $t_{fin} \rightarrow \infty$, $E_{fin} \rightarrow E_0$ (the asymptotic values of the energies, E_0, are reported in Table S4).

In order to verify that our Stochastic Dynamics results are not system size dependent, we increased the box size as well as the number of nanoparticles while keeping constant the volume fraction. Specifically, we tested the system size independence in suspensions of particle volume fractions, Φ = 2% and Φ = 0.5% . Therefore, we systematically carried out SD simulations of suspensions with 4000, 8000 and 16000 nanoparticles. The results are collected in Fig. S12, where the calculated physical quantities are compared with those one of the original system, composed of 2000 nanoparticles.

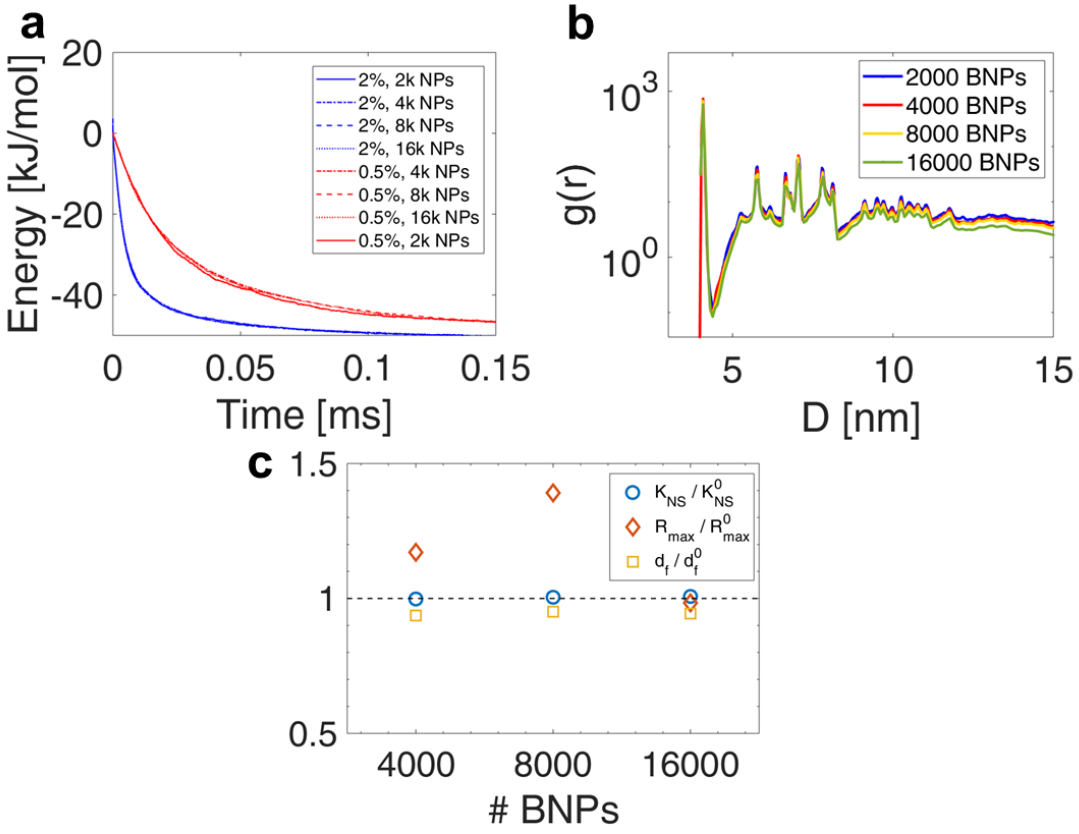

Fig. S12: (a) Total energy per single NP calculated using stochastic dynamics simulations of neutral BNPs in aqueous solutions. Two NP volume fraction are considered, namely Φ = 2% and Φ = 0.5%. For each volume fraction considered, suspensions of 2000 (2k), 4000 (4k), 8000 (8k) and 16000 (16k) NPs are simulated and compared in terms of the total energy per single NP. (b) Radial distribution functions, (g(r)), of suspended neutral BNPs at volume fractions Φ = 2%. The g(r) is computed in suspensions of 2000 (2k), 4000 (4k), 8000

(8k) and 16000 (16k) BNPs. (c) Ratio of the thermal conductivity of nanosuspension (k_{NS}), maximum cluster radius (R_{max}) and average fractal dimension parameter (d_f) with respect to the reference values of k_{NS}^0, R_{max}^0 and d_f^0 corresponding to a suspension of 2000 BNPs. The values of k_{NS}/k_{NS}^0, R_{max}/R_{max}^0 and d_f/d_f^0 are computed for nanosuspensions of 4000, 8000 and 16000 BNPs concentrated at Φ = 2%.

As Fig. S12 (a) shows, the potential energy per NP of the above-mentioned configurations is completely independent from the system size, while it only depends on the NP volume fractions. The radial distribution functions, g(r), plotted in Fig. S12 (b) and correspond to the NPs in the four configurations (#NPs = 2000, #NPs = 4000, #NPs = 8000, #NPs = 16000) also exhibit a congruent shape and analogous peaks, thereby showing that the dendritic structure is recovered independently from the system size.

The influence of the system size is finally investigated in terms of thermal conductivity of nanosuspension (k_{NS}), maximum cluster radius (R_{max}) and average fractal dimension parameter (d_f). Such values are compared with those one calculated in the reference configuration characterized by a suspension of 2000 NPs. As Fig. S12 (c) highlights, the system size does not affect the thermal conductivity results and the fractal dimension parameters of the resulting cluster for a given volume fraction. Note that, besides the interaction potential, the final shape of the aggregates is also determined by the intrinsic randomness of the SD algorithm, which explains the small differences in the value of the radius of the larger aggregate in each configuration.

4.2. Time Evolution of the NP Clusters

For each volume fraction, we carried out the cluster analysis at several frames along the simulation trajectories, thereby providing a global picture of the kinetics of NP aggregation. Simulation snapshots of the self-assembly process are shown in Fig. S13 (a-d), at various time steps (t = 0 ms, t = 0.007 ms, t = 0.023 ms, and t = 0.055 ms). In the early stage of the self-assembly process, the NP suspension contains primarily small clusters. After a few μs, the nanoparticles begin to form bigger clusters of different fractal dimensions. Finally, at t = 0.055 ms, a few large-size clusters can be observed in the simulation box. A more quantitative description of the kinetics of NP aggregation is presented in Fig. S13 (e). The plot shows the time evolution of the number of clusters of various sizes, from t = 0 ms to t = 0.055 ms. As expected, initially (t < 0.01 ms), the number of clusters with less than 5 NPs (purple curve) decreases, because these small aggregates progressively form clusters containing more NPs, i.e., clusters consisting of 6 to 20 NPs (green curve) and 21 to 50 NPs (blue curve). However, the life-time of these larger aggregates decreases because they self-assemble into bigger structures consisting of more than 50 NPs. After about 0.0045 ms, the kinetics of NP aggregation slows down, and the number of clusters of a given size plateaus to a constant value (see orange and black curves in Fig. S13(e)).

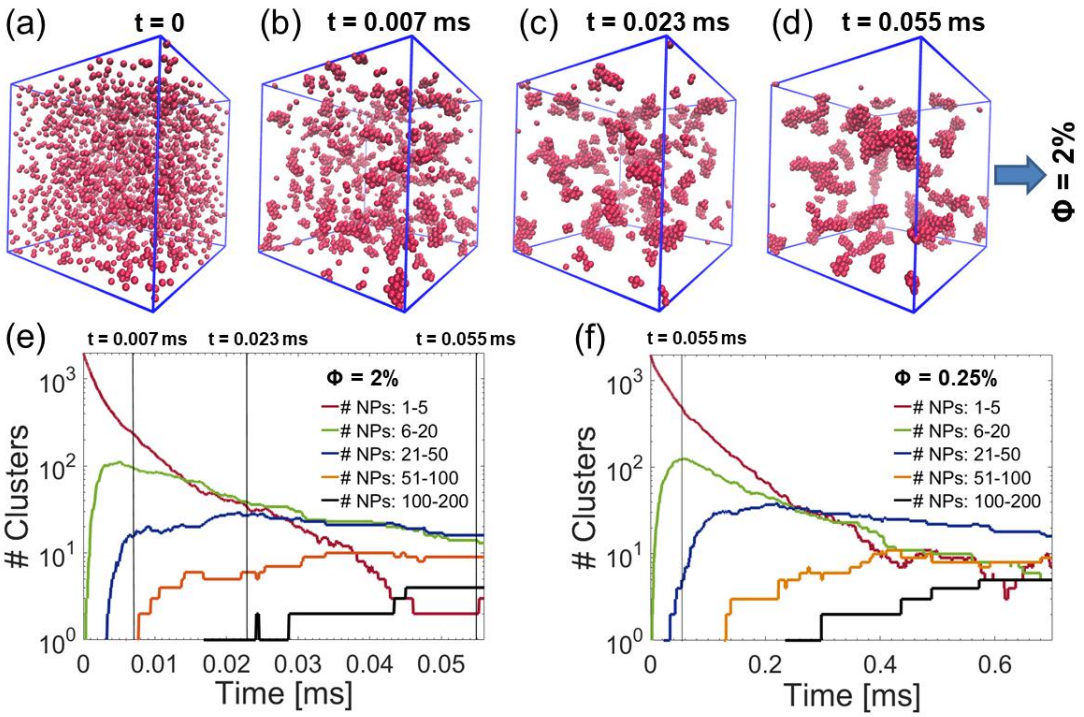

Fig. S13: The aggregation state of suspended nanoparticles (Φ = 2%) at (a) t = 0 ms, (b) t = 0.007 ms, (c) t = 0.023 ms, and (d) t = 0.055 ms. The number of clusters (# Clusters) of a specific size (# NPs) is plotted during the first (e) 0.06 ms and (f) 0.7ms of the trajectory for a NP suspension with Φ = 2% and Φ = 0.25%, respectively. Note that the radius of the neutral BNP is equal to 2 nm.

In summary, Fig. S13 (e) illustrates the possible scenarios involved in NP cluster formation: on the one hand, the growth of NP clusters results from the progressive addition of single-dispersed NPs which gradually decrease in number, and on the other hand, the aggregation cohesion of medium-size NP clusters can directly form a bigger one. Fig. S13 (f) displays the time-dependent size distribution of the NP aggregates when Φ = 0.25%, from t = 0 ms to t = 0.7 ms. Although the trends are similar to those observed when Φ = 2%, the characteristic times for self-assembly are remarkably different (compare the x-axes in Fig. S13 (e) and Fig. S13 (f)). For example, when Φ = 2% and t = 0.055 ms, the aggregation of NPs has almost reached steady state (see Fig. S13 (e)). On the other hand, when Φ = 0.25% and t = 0.055 ms (see Fig. S13 (f)), the NP self-assembly process is in its early stages.

5. Prediction of the Thermal Conductivity by Coupling the DLVO and the Kinetic Aggregation Theory

In the main text, we have shown how we combined the adaptation of the Bruggeman (BG) model[S32] to the cluster analysis of our multi-scale method in order to predict the thermal conductivity of NP suspensions. We validated our approach by comparing the results of the thermal conductivity with (i) experimental data, and (ii) theoretically predicted values (Figure 7 in the main text). In this section, we describe how we calculated the thermal conductivity in case (ii). Specifically, instead of considering the distribution of NP clusters obtained by SD simulations, we coupled the DLVO theory

and the kinetic aggregation theory to calculate the dynamics and the characteristic time of NP aggregation. Then, we used the adaptation of the BG model to compute the thermal conductivity. The evolution of NP aggregation was predicted by applying the Smoluchowski kinetic theory[S33] which involves a set of population balance equations (PBEs) describing the evolution of the number of clusters, N_k, with size *k* at time *t*. Assuming that the coagulation starts from a homogeneous dispersion of nanoparticles, the PBEs reduce to:

$$\frac{dN_k}{dt} = \frac{1}{2}\sum_{i=1}^{k-1} K_{ij} N_i N_j - \sum_{i=1}^{\infty} K_{ki} N_i N_k, \tag{15}$$

where K_{ij} is the agglomeration frequency and is a function of the stability ratio W_{ij}[S34]:

$$W_{ij} = 2\int_0^{\infty} \frac{B(u)}{(2+u^2)} \exp\left(\frac{U_{tot,ij}}{k_B T}\right) dr, \tag{16}$$

where k_B is the Boltzmann constant, T is the absolute temperature, $U_{tot,ij}$ is the total interaction energy between particles i and j, and $B(u)$ is the hydrodynamic resistance function given by $B(u) = (6u^2 + 13u + 2)/(6u^2 + 4u)$, where $u = h/R_p$ is a dimensionless parameter based on the surface-surface particle distance, h, and the NP radius, R_p. It is worth noting that because the fragmentation of the NP clusters is considered negligible in the absence of shear, we carried out the present study assuming that only aggregation occurs between clusters. The stability ratio was evaluated by introducing, as interaction potential U_{tot} in Eq. 16, the classical DLVO potential energy corresponding to the BNPs. In particular, Eq. 2 in the main text is used to calculate the U_{tot} of BNPs when the pH is close to the isoelectric point (pH = IEP). On the other hand, a summation of Eqs. 2 and 4 in the main text is applied to compute U_{tot} between BNPs suspended in aqueous solutions with pH ≠ IEP. We point out that here we used the experimental zeta potential values as a function of alumina nano-suspension pH[S35] to predict the NP surface potential (ψ_0 in Eq. 4 of the main text). Knowing the stability ratio W_{ij}, the time for NP aggregation was calculated as follows[S34]:

$$t_p = \frac{\pi \mu {R_p}^3 W}{k_B T \Phi}, \tag{17}$$

where μ is the viscosity of the fluid, R_p = 2 nm is the NP radius, and Φ is the NP volume fraction. Subsequently, we evaluated the concentration of NPs inside the clusters as follows[S34]:

$$\Phi_{in} = \left(R_a/R_p\right)^{d_f-3} = \left(1 + t/t_p\right)^{(d_f-3)/d_f}, \tag{18}$$

where d_f was assumed to be constant and equal to 1.8 in the case of fast diffusion-limited aggregation (pH = IEP), and to 2.5 in the case of reaction-limited aggregation kinetics (pH = 5 and pH = 1)[S36]. We specify that, differently from the cluster analysis based on our SD simulations, here, the fractal dimension parameters are assumed to be constant for all the NP clusters inside the specific nano-suspension. Finally, the values of Φ_{in} corresponding to the nano-suspensions considered were included in the adapted BG model (Eq. 9 and 10 of the main text) to calculate the theoretical thermal conductivity values. The black curves in Fig. S14 show the theoretically predicted values, k_{NS}/k_{bf},

obtained following the previously described approach. In order to include a window of values corresponding to NP suspensions at different chemical conditions, k_{NS}/k_{bf} was calculated at three different solution pHs, namely, (a) pH = IEP, (b) pH = 5, and (c) pH = 1. The solid curves in Fig. S14 show the values of k_{NS}/k_{bf} after 12 hours from the initial condition of mono-disperse NPs. This time can be considered as reasonable for the experimental measurements carried out here[S37]. The dashed curves, instead, indicate the results of k_{NS}/k_{bf} related to the limiting condition of $\Phi_{in} = \Phi$, namely, when the NPs are completely aggregated. It is interesting to see that when the solid curve is above the dashed curve (see Fig. S14), the nano-suspensions reach a completely-aggregated state before 12 h. On the other hand, the complete aggregated state is obtained after 12 hours. Table S6 reports the characteristic time corresponding to the limiting condition of $\Phi_{in} = \Phi$ (dashed curve in Fig. S14). As Fig. S14 shows, although the relative thermal conductivity increases as the aggregation becomes more intense, until complete aggregation takes place, such theoretical values remain very far from the experimental predictions.

Characteristic Time [s]				
	$\Phi = 0.2\ \%$	$\Phi = 0.5\ \%$	$\Phi = 1\ \%$	$\Phi = 2\ \%$
pH = IEP	0.0233	0.0021	$3.376 \cdot 10^{-4}$	$6.147 \cdot 10^{-5}$
pH = 5	$1.3 \cdot 10^{9}$	$4.1 \cdot 10^{6}$	$5.2 \cdot 10^{4}$	873.59
pH = 1	$1.58 \cdot 10^{11}$	$4.86 \cdot 10^{8}$	$6.14 \cdot 10^{6}$	$1.03 \cdot 10^{5}$

Table S5: Characteristic time to obtain fully aggregated nano-suspensions ($\Phi_{in} = \Phi$), as a function of solution pH and NP volume fraction, Φ. The characteristic time for complete aggregation is calculated according to the DLVO-based kinetic aggregation theory (see Eqs. 15, 16 and 17).

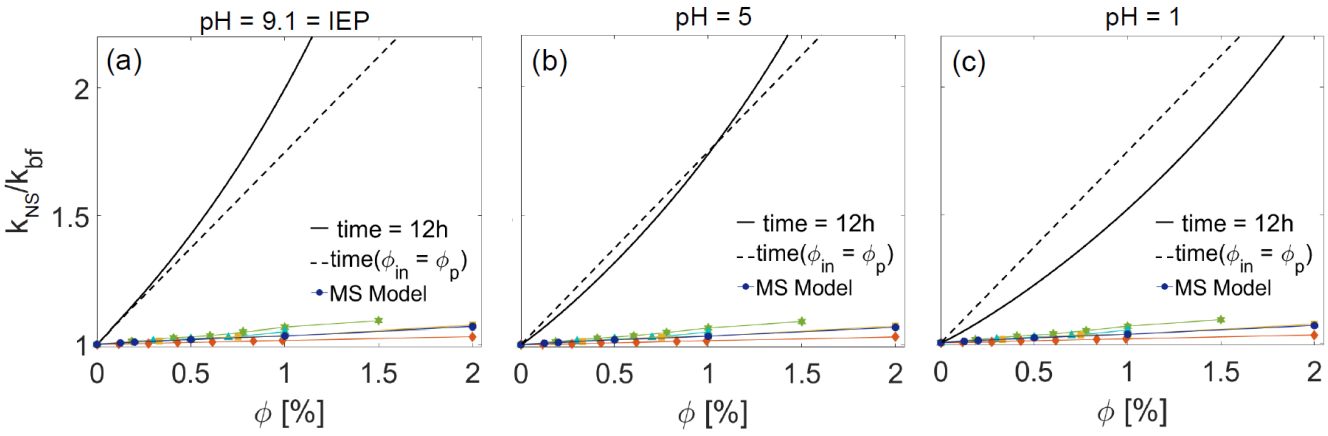

Fig. S14: (a-c) Relative thermal conductivity, k_{NS}/k_{bf}, of suspended alumina NPs in water as a function of the particle volume fraction, Φ, at (a) pH = 9.1, (b) pH = 5, and (c) pH = 1. The black solid and dashed curves represent the predictions of k_{NS}/k_{bf} using the DLVO theory and the kinetic aggregation theory discussed above, respectively. The thermal conductivity values are calculated after 12 hours (black solid curves), as well as when the suspensions have reached a completely-aggregated state, namely when $\Phi_{in} = \Phi$ (black dashed curves). The blue dots are calculated following the multi-scale (MS) model presented in the main text. The values of k_{NS}/k_{bf} are also compared with the experimental data reported in the literature: the orange diamonds from[S38], the green stars are from[S39], the yellow squares from[S40], and the light blue triangles from[S41].

5.2 The Influence of Kapitza Resistance on the Thermal Conductivity Calculation

The presence of a thermal resistance, also known as Kapitza resistance, at solid-liquid interface plays a crucial role in several thermal transport phenomena and it has been largely studied and discussed in the literature[S45,S46]. In the field of nanoparticle suspensions, Nan[S46] and Putnam[S47] dealt with the effect of Kapitza resistance in well-dispersed NP suspensions. However, their models based on the fundamental assumption of a moderate concentration of NPs inside the clusters and the absence of elongated dendrites in the cluster structural shape. Consequently, such models show remarkable deficiencies if applied to our study cases which are often characterized by a strong kinetic of aggregation.

However, in order to roughly estimate the effect of the Kapitza resistance on the thermal conductivity results, we modified the effective thermal conductive of the alumina NPs, $k_{p,eff}$, according to the following model developed by Ebrahimi[S48]:

$$\mathrm{k_{p,eff}} = \frac{2\mathrm{R}}{\mathrm{R_K} + 2\mathrm{R}/\mathrm{k_p}}, \tag{19}$$

where k_p is the alumina NP thermal conductivity and $\mathrm{R_K} = 5 \cdot 10^8\ \mathrm{Km^2/W}$ is the particle-water thermal resistance derived by Timofeeva[S38] after fitting the experimental results on alumna NP suspensions. Therefore, we included the values of $\mathrm{k_{p,eff}}$ in Eq. 9 of the main text, and we collected the results in Fig. S15.

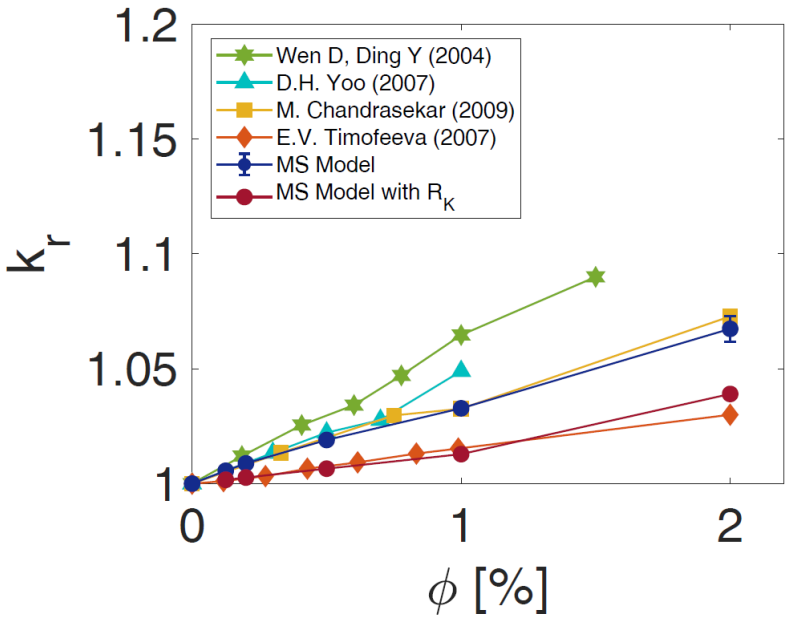

Fig. S15: Relative thermal conductivity ($\mathbf{k_r = k_{NS}/k_{bf}}$) of suspended alumina BNPs in water as a function of the particle volume fraction, Φ. The blue and red dots represent the results obtained by applying, respectively, the MS Model and the MS Model coupled with the effect of thermal resistance $\mathbf{R_K}$.

Comparing the results in Fig. S15, we notice that the two approaches (MS Model and MS Model with $\mathrm{R_K}$) present similar trends, and the relative error remains below 3%. However, the presence of

aggregation phenomena and the consequently modification of the solid-liquid interface ration could bring to notable modulation of the R_K.

6. Theoretical Prediction of the Viscosity and Specific Heat Capacity

To calculate the viscosity of the nano-suspension, we considered a widely adopted model first proposed by Krieger and Dougherty[S42]. Although this is one of the few theories that incorporates particle aggregation in the dispersion, the assumptions of limited-aggregation kinetics and regular cluster shape limit its use for any volume fraction. Accordingly, in the viscosity calculation, we excluded suspensions having 1% and 2% particle volume fractions, where significant NP aggregation phenomena take place. After evaluating the internal volume fraction of the aggregates, Φ_{in} using Eq. 18, the viscosity of each suspension, characterized by a specific cluster i, is expressed as follows[S43]:

$$\mu_{NS_i} = \mu_{bf}\left(1 - \frac{\Phi_{a_i}}{\Phi_m}\right)^{-\eta\Phi_m}, \tag{19}$$

where η is the intrinsic viscosity and Φ_m are 2.5 and 0.73, respectively[S43]. Note that Φ_m is strongly related to the NP packing in the aggregate. Similar to the evaluation of the thermal conductivity of the NP suspension, the overall viscosity of the nano-suspension, for a given particle volume fraction, is given by:

$$\mu_{NS} = \frac{\sum_{i=1}^{N_c} \mu_{NS_i}}{N_c}, \tag{20}$$

where N_c is the number of fictitious suspensions, each consisting of identical aggregates. The viscosity calculation presented above includes one of the few theoretical models reported in literature and accounting for the internal volume fraction in the aggregates. However, we point out that the values of viscosity were obtained by keeping constant the intrinsic viscosity and maximum concentration, respectively η and Φ_m, which are instead related to the cluster geometry and the actual applied shear rate. As a consequence, in accordance to the model proposed, we assumed the growth of well-packed aggregates neglecting for the effective dendritic shape of each cluster and overestimating Φ_m. A correction of the present theory according to the actual shape of the cluster would significantly enhance its predictive ability, however this is beyond the scope of this paper.

Finally, to calculate the specific heat capacity of the NP suspension, we utilized the following volume-fraction averaged equation[S44]:

$$c_{p,NS} = \frac{(1-\Phi)(\rho c_p)_{bf} + \Phi(\rho c_p)_p}{\rho_{NS}}, \tag{21}$$

where $(\rho c_p)_{bf}$ = 4166.5 kJ/K·m^3 and $(\rho c_p)_p$ = 3056.7 kJ/K·m^3 are the base fluid and alumina volumetric heat capacities, respectively. The resulting relative viscosity and Prandtl number ($Pr = c_{p,NS}\, k_{NS}/\mu_{NS}$) of the nano-suspensions at the three volume fractions considered are

reported in Table S6. As expected, the observed increase in the thermal conductivity with NP volume fraction (see Fig. S15) is accompanied by a concomitant increase in viscosity. This finding indicates the need for a trade-off in the use of nano-suspensions in thermal transport applications. Indeed, attaining desirable higher thermal conductivities requires using NP suspensions having higher viscosities, which may be practically detrimental.

Φ [%]	μ_{NS}/μ_{bf}	Pr
0.125	1.02±0.01	4.2
0.2	1.04±0.01	4.3
0.5	1.22±0.2	4.8

Table S6: Relative thermal conductivity, k_{NS}/k_{bf}, and viscosity, μ_{NS}/μ_{bf}, of the NP suspensions computed using the SD cluster analysis as an input. As explained in the text (see also Reference S43), the viscosities were not calculated for NP suspensions having values of Φ = 1% and Φ = 2%.

References

S1. Zaera, F. Nanostructured materials for applications in heterogeneous catalysis. Chemical Society Reviews 2013, 42, 2746-2762.

S2. Zhang, L.; Guo, Y.; Hassan, V. V.; Tang, K.; Foad, M. A.; Woicik, J. C.; Pianetta, P.; Robertson, J.; McIntyre, P. C. Interface Engineering for Atomic Layer Deposited Alumina Gate Dielectric on SiGe Substrates. ACS Applied Materials & Interfaces 2016, 8, 19110-19118.

S3. Abdullah, A.; Lindsay, K. Marangoni convection in a thin layer of nanofluid: Application to combinations of water or ethanol with nanoparticles of alumina or multiwalled carbon nanotubules. International Journal of Heat and Mass Transfer 2017, 104, 693-702.

S4. Hosseini, S. H.; Taghizadeh-Alisaraei, A.; Ghobadian, B.; Abbaszadeh-Mayvan, A. Effect of added alumina as nano-catalyst to diesel-biodiesel blends on performance and emission characteristics of CI engine. Energy 2017, 124, 543-552.

S5. Hass, K. C.; Schneider, W. F.; Curioni, A.; Andreoni, W. The chemistry of water on alumina surfaces: Reaction dynamics from first principles. Science 1998, 282, 265-268.

S6. Blonski, S.; Garofalini, S. Molecular dynamics simulations of α-alumina and γ-alumina surfaces. Surface Science 1993, 295, 263-274.

S7. Argyris, D.; Ho, T.; Cole, D. R.; Striolo, A. Molecular dynamics studies of interfacial water at the alumina surface. The Journal of Physical Chemistry C 2011, 115, 2038-2046.

S8. Eng, P. J.; Trainor, T. P.; Brown Jr, G. E.; Waychunas, G. A.; Newville, M.; Sutton, S. R.; Rivers, M. L. Structure of the hydrated α-Al2O3 (0001) surface. Science 2000, 288, 1029-1033.

S9. Zhang, L.; Li, H.; Chen, F.; Zhang, D.; Wu, M.; Pan, B.; Xing, B. New insights provided by solvent relaxation NMR-measured surface area in liquids to explain phenolics sorption on silica nanoparticles. Environmental Science: Nano 2017, 4, 577-584.

S10. Connolly, M. L. Solvent-accessible surfaces of proteins and nucleic acids. Science 1983, 221, 709-713.

S11. Cygan, R. T.; Liang, J.-J.; Kalinichev, A. G. Molecular models of hydroxide, oxyhydroxide, and clay phases and the development of a general force field. The Journal of Physical Chemistry B 2004, 108, 1255-1266.
S12. Senftle, T. P.; Hong, S.; Islam, M. M.; Kylasa, S. B.; Zheng, Y.; Shin, Y. K.; Junkermeier, C.; Engel-Herbert, R.; Janik, M. J.; Aktulga, H. M.; Verstraelen, T.; Grama, A.; van Duin, A. C. T. The ReaxFF reactive force-field: development, applications and future directions. npj Computational Materials 2016, 2, 15011.
S13. Berendsen, H.; Grigera, J.; Straatsma, T. The missing term in effective pair potentials. Journal of Physical Chemistry 1987, 91, 6269-6271.
S14. Nosé, S.; Klein, M. Constant pressure molecular dynamics for molecular systems. Molecular Physics 1983, 50, 1055-1076.
S15. Parrinello, M.; Rahman, A. Polymorphic transitions in single crystals: A new molecular dynamics method. Journal of Applied physics 1981, 52, 7182-7190.
S16. Israelachvili, J.; Wennerström, H. Role of hydration and water structure in biological and colloidal interactions. Nature 1996, 379, 219.
S17. Pashley, R. DLVO and hydration forces between mica surfaces in Li+, Na+, K+, and Cs+ electrolyte solutions: a correlation of double-layer and hydration forces with surface cation exchange properties. Journal of Colloid and Interface Science 1981, 83, 531-546.
S18. Derjaguin, B.; Landau, L. The theory of stability of highly charged lyophobic sols and coalescence of highly charged particles in electrolyte solutions. Acta Physicochim. URSS 1941, 14, 633-52.
S19. Verwey, E.; Overbeek, J. T. G. Theory of the stability of lyophobic colloids. Journal of Colloid Science 1955, 10, 224-225.
S20. Israelachvili, J. N. Intermolecular and Surface Forces; Academic press, 2011.
S21. Sader, J. E.; Carnie, S. L.; Chan, D. Y. Accurate analytic formulas for the double layer interaction between spheres. Journal of Colloid and Interface Science 1995, 171, 46-54.
S22. Hogg, R.; Healy, T. W.; Fuerstenau, D. Mutual coagulation of colloidal dispersions. Transactions of the Faraday Society 1966, 62, 1638-1651.
S23. Belloni, L. Ionic condensation and charge renormalization in colloidal suspensions. Colloids and Surfaces A: Physicochemical and Engineering Aspects 1998, 140, 227-243.
S24. Alexander, S.; Chaikin, P.; Grant, P.; Morales, G.; Pincus, P.; Hone, D. Charge renormalization, osmotic pressure, and bulk modulus of colloidal crystals: Theory. The Journal of chemical physics 1984, 80, 5776-5781.
S25. Boon, N.; Guerrero-García, G. I.; Van Roij, R.; De La Cruz, M. O. Effective charges and virial pressure of concentrated macroion solutions. Proceedings of the National Academy of Sciences 2015, 112, 9242-9246.
S26. Diehl, A.; Levin, Y. Effective charge of colloidal particles. The Journal of chemical physics 2004, 121, 12100_12103.
S27. Linse, P. Structure, phase stability, and thermodynamics in charged colloidal solutions. The Journal of Chemical Physics 2000, 113, 4359-4373.
S28. Milner, S. T.; Witten, T.; Cates, M. Theory of the grafted polymer brush. Macro- molecules 1988, 21, 2610-2619.

S29. Xu, Z.; Yang, X.; Yang, Z. A molecular simulation probing of structure and interaction for supramolecular sodium dodecyl sulfate/single-wall carbon nanotube assemblies. Nano letters 2010, 10, 985-991.
S30. Lemons, D. S.; Gythiel, A. Paul Langevin's 1908 paper ''On the Theory of Brownian Motion'' ["Sur la théorie du mouvement brownien'', CR Acad. Sci.(Paris) 146, 530-533 (1908)]. American Journal of Physics 1997, 65, 1079-1081.
S31. Edward, J. T. Molecular volumes and the Stokes-Einstein equation. Journal of Chemical Education 1970, 47, 261.
S32. Bruggeman, V. D. Berechnung verschiedener physikalischer Konstanten von heterogenen Substanzen. I. Dielektrizitätskonstanten und Leitfähigkeiten der Mischkörper ausisotropen Substanzen. Annalen der physik 1935, 416, 636-664.
S33. Smoluchowski, M. v. Versuch einer mathematischen Theorie der Koagulationskinetik kolloider Lösungen. Zeitschrift für physikalische Chemie 1918, 92, 129-168.
S34. Prasher, R.; Phelan, P. E.; Bhattacharya, P. Effect of aggregation kinetics on the thermal conductivity of nanoscale colloidal solutions (nanofluid). Nano Letters 2006, 6, 1529-1534.
S35. Kim, D.; Kim, H.; Lee, J. Dependence of the rheological behaviour of electrostatically stabilized alumina slurries on pH and solid loading. Journal of materials science 1998, 33, 2931-2935.
S36. Witten Jr, T.; Sander, L. M. Diffusion-limited aggregation, a kinetic critical phenomenon. Physical review letters 1981, 47, 1400.
S37. Das, S. K.; Putra, N.; Thiesen, P.; Roetzel, W. Temperature dependence of thermal conductivity enhancement for nanofluids. Journal of heat transfer 2003, 125, 567-574.
S38. Timofeeva, E. V.; Gavrilov, A. N.; McCloskey, J. M.; Tolmachev, Y. V.; Sprunt, S.; Lopatina, L. M.; Selinger, J. V. Thermal conductivity and particle agglomeration in alumina nanofluids: experiment and theory. Physical Review E 2007, 76, 061203.
S39. Wen, D.; Ding, Y. Experimental investigation into convective heat transfer of nanofluids at the entrance region under laminar flow conditions. International journal of heat and mass transfer 2004, 47, 5181-5188.
S40. Chandrasekar, M.; Suresh, S.; Bose, A. C. Experimental investigations and theoretical determination of thermal conductivity and viscosity of Al2O3/water nanofluid. Experimental Thermal and Fluid Science 2010, 34, 210-216.
S41. Yoo, D.-H.; Hong, K.; Yang, H.-S. Study of thermal conductivity of nanofluids for the application of heat transfer fluids. Thermochimica Acta 2007, 455, 66-69.
S42. Krieger, I. M.; Dougherty, T. J. A mechanism for non-Newtonian flow in suspensions of rigid spheres. Transactions of the Society of Rheology 1959, 3, 137-152.
S43. Starov, V.; Zhdanov, V.; Meireles, M.; Molle, C. Viscosity of concentrated suspensions: influence of cluster formation. Advances in colloid and interface science 2002, 96, 279-293.
S44. Bigdeli, M. B.; Fasano, M.; Cardellini, A.; Chiavazzo, E.; Asinari, P. A review on the heat and mass transfer phenomena in nanofluid coolants with special focus on automotive applications. Renewable and Sustainable Energy Reviews 2016, 60, 1615-1633.

S45. Tascini, A. S.; Armstrong, J.; Chiavazzo, E.; Fasano, M.; Asinari, P.; Bresme, F. Thermal transport across nanoparticle-fluid interfaces: the interplay of interfacial curvature and nanoparticle-fluid interactions. Physical Chemistry Chemical Physics 2017, 19, 3244-3253.

S46. Nan, C.-W.; Birringer, R.; Clarke, D. R.; Gleiter, H. Effective thermal conductivity of particulate composites with interfacial thermal resistance. Journal of Applied Physics 1997, 81, 6692-6699.

S47. Putnam, S. A.; Cahill, D. G.; Ash, B. J.; Schadler, L. S. High-precision thermal conductivity measurements as a probe of polymer/nanoparticle interfaces. Journal of Applied Physics 2003, 94, 6785-6788.

S48. Ebrahimi, A.; Rikhtegar, F.; Sabaghan, A.; Roohi, E. Heat transfer and entropy generation in a microchannel with longitudinal vortex generators using nanofluids. Energy 2016, 101, 190-201.